Gyrokinetic Studies of Ion Temperature Gradient Turbulence and Zonal Flows in Helical Systems

Hideo SUGAMA[1,2], Tomo-Hiko WATANABE[1,2], and Sergi FERRANDO-MARGALET[1)]

[1)]*National Institute for Fusion Science, Toki 509-5292, Japan*

[2)]*Graduate School for Advanced Studies (Sokendai), Toki 509-5292, Japan*

Gyrokinetic theory and simulation results are presented to investigate regulation of ion temperature gradient (ITG) turbulence due to $\mathbf{E}\times\mathbf{B}$ zonal flows in helical systems. In order to examine effects of changes in helical magnetic configuration on anomalous transport and zonal flows, magnetic field parameters representing the standard and inward-shifted configurations of the Large Helical Device (LHD) [O. Motojima, N. Ohyabu, A. Komori, *et al*., Nucl. Fusion **43**, 1674 (2003)] are used. The linear gyrokinetic analyses show that the largest growth rate of the linear ITG instability for the inward-shifted configuration is higher than that in the standard one while, for the former case, zonal flows generated by given sources decay more slowly because of lower radial drift velocities of helical-ripple-trapped particles than for the latter as theoretically predicted. It is shown from the gyrokinetic Vlasov simulation of the ITG turbulence that, in spite of the higher ITG-mode growth rate, the inward-shifted plasma takes a smaller average value of the ion thermal diffusivity in the steady turbulent state with a higher zonal-flow level. These results imply that neoclassical optimization contributes to reduction of the anomalous transport by enhancing the zonal-flow level and give a physical explanation for the confinement improvement observed in the LHD experiments with the inward plasma shift. When equilibrium radial electric fields produce poloidal $\mathbf{E}\times\mathbf{B}$ rotation of helically-trapped particles with reduced radial displacements, further enhancement of zonal flows and resultant transport reduction are theoretically expected.

Keywords: zonal flow, ITG turbulence, gyrokinetic simulation, helical system, LHD

1 Introduction

In fusion science, numerous theoretical and experimental works have been done on zonal flows which are now well known to play a critical role in regulation of turbulent transport in plasmas [1, 2]. Therefore, in order to improve plasma confinement in helical systems, where various geometrical configurations are explored [3, 4, 5, 6, 7], it is very important to elucidate effects of magnetic geometry on both microinstabilities and zonal flows. This work presents results from gyrokinetic theory and simulation to investigate regulation of ion temperature gradient (ITG) turbulence due to $\mathbf{E}\times\mathbf{B}$ zonal flows in helical systems.

It was shown in our previous papers [8, 9, 10, 11] that, in helical systems, zonal flows can be maintained for a longer time by reducing the radial drift velocities of particles trapped in helical ripples. This implies a possibility that helical configurations optimized for reducing the neoclassical transport can enhance zonal flows and accordingly lower the turbulent transport as well because the neoclassical particle and heat fluxes are also decreased by slowing down the radial drift of helical-ripple-trapped particles. In fact, it is observed in the Large Helical Device (LHD) [12] that not only neoclassical but also anomalous transport is reduced by the inward plasma shift [13] which decreases the radial particle drift but increases the unfavorable magnetic curvature to destabilize pressure-gradient-driven instabilities such as ITG modes. This reduction of anomalous transport by neoclassical optimization is a very attractive property of helical systems to recent researches on advanced concepts of helical devices [3, 4, 5, 6, 7]

It was shown by the ITG turbulence simulation in our previous work [10, 11], in which model helical fields for the standard and inward-shifted LHD configurations were used in the gyrokinetic Vlasov (GKV) code [14], that the turbulent ion thermal transport in the inward-shifted model, which has larger growth rates of the ITG stability, was considerably regulated by the zonal flows to a level comparable to the standard case although the thermal diffusivity χ_i for the inward-shifted case was slightly but still larger than for the standard case. However, in the recent GKV simulation with more accurate configuration models installed [15], we find that further stronger zonal-flow generation occurs and makes χ_i smaller for the inward-shifted configuration [16].

Recently, Mynick and Boozer [17] predicted by using the action-angle formalism that the collisionless residual zonal-flow level will be enhanced when the equilibrium radial electric field causes helical-ripple-trapped particles to follow closed poloidal orbits with small radial displacements. Here, our gyrokinetic theory of zonal-flow response is also extended to analytically derive detailed expressions for the effects of the equilibrium electric field on zonal flows in helical systems.

author's e-mail: sugama.hideo@LHD.nifs.ac.jp

2 Basic Equations

The nonlinear gyrokinetic equation for the perturbed ion gyrocenter distribution function $f_{i\mathbf{k}_\perp}$ with the wave number vector $\mathbf{k}_\perp$ perpendicular to the magnetic field $\mathbf{B}$ is written as

$$\begin{aligned}\left(\frac{\partial}{\partial t}+v_\parallel\mathbf{b}\cdot\nabla+i\omega_{Di}\right)f_{\mathbf{k}_\perp}\\ =\ (-v_\parallel\mathbf{b}\cdot\nabla-i\omega_{Di}+i\omega_{*Ti})\left(F_0J_0(k_\perp\rho)\frac{e\phi_{\mathbf{k}_\perp}}{T_i}\right)\\ +\frac{c}{B}\sum_{\mathbf{k}'_\perp+\mathbf{k}''_\perp=\mathbf{k}_\perp}[\mathbf{b}\cdot(\mathbf{k}'_\perp\times\mathbf{k}''_\perp)]J_0(k'_\perp\rho)\phi_{\mathbf{k}'_\perp}f_{i\mathbf{k}''_\perp},\end{aligned} \tag{1}$$

where F_0 is the local ion equilibrium distribution function that takes the Maxwellian form, $J_0(k_\perp\rho)$ is the zeroth-order Bessel function, $\rho = v_\perp/\Omega_i$ is the ion gyroradius, and $\Omega_i = eB/(m_ic)$ is the ion gyrofrequency. The two frequencies ω_{Di} and ω_{*i} are defined by $\omega_{Di} = \mathbf{k}_\perp\cdot\mathbf{v}_{Di}$ and by $\omega_{*Ti} = \omega_{*i}[1+\eta_i\{m_iv^2/2T_i-3/2\}]$ respectively, where $\mathbf{v}_{Di} \equiv (c/eB)\mathbf{b}\times(e\nabla\Phi+\mu\nabla B+m_iv_\parallel^2\mathbf{b}\cdot\nabla\mathbf{b})$ is the ion gyrocenter drift velocity, $\omega_{*i} \equiv \mathbf{k}_\perp\cdot(\mathbf{b}\times\nabla r)(cT_i/eB)(d\ln n_0/dr)$ is the ion diamagnetic frequency, and $\eta_i \equiv L_n/L_{Ti}$ is the ratio of the density gradient scale length $L_n \equiv -1/(d\ln n_0/dr)$ to the ion temperature gradient scale length $L_{Ti} \equiv -1/(d\ln T_i/dr)$. In Eq. (1), $f_{i\mathbf{k}_\perp}$ is regarded as a function of the kinetic energy $w \equiv \frac{1}{2}m_iv^2$, the magnetic moment $\mu \equiv m_iv_\perp^2/(2B)$, and the toroidal coordinates (r,θ,ζ), where r, θ, and ζ denote the flux surface label, the poloidal angle, and the toroidal angle, respectively. A closed system of equations to determine the perturbed ion distribution function $f_{i\mathbf{k}_\perp}$ and the electrostatic potential $\phi_{\mathbf{k}_\perp}$ in the ITG turbulence are given by Eq. (1) and the quasineutrality condition,

$$\int d^3v\ J_0f_{i\mathbf{k}_\perp}-n_0\frac{e\phi_{\mathbf{k}_\perp}}{T_i}\left[1-\Gamma_0(b)\right]=n_0\frac{e}{T_e}\left(\phi_{\mathbf{k}_\perp}-\langle\phi_{\mathbf{k}_\perp}\rangle\right), \tag{2}$$

where $\langle\cdots\rangle$ represents the flux-surface average and $\Gamma_0(b)$ is defined by $\Gamma_0(b) \equiv I_0(b)e^{-b}$ with the zeroth-order modified Bessel function $I_0(b)$ and $b \equiv k_\perp^2T_i/(m_i\Omega_i^2)$.

The magnetic field is written as $\mathbf{B} = \nabla\psi(r)\times\nabla(\theta-\zeta/q(r))$, where $2\pi\psi(r)$ is equal to the toroidal flux within the flux surface labeled r and $q(r)$ represents the safety factor. In the present work, the radial coordinate r is defined by $\psi = B_0r^2/2$. Following Shaing and Hokin [18], we here consider helical systems with the magnetic field strength B written by

$$\begin{aligned}B/B_0 &= 1-\epsilon_{00}(r)-\epsilon_{10}(r)\cos\theta-\epsilon_{L0}(r)\cos(L\theta)\\ &\quad-\sum_{|n|\le n_{max}}\epsilon_h^{(n)}(r)\cos\{(L+n)\theta-M\zeta\}\\ &= 1-\epsilon_{00}(r)-\epsilon_T(r,\theta)\\ &\quad-\epsilon_H(r,\theta)\cos\{L\theta-M\zeta+\chi_H(\theta)\},\end{aligned} \tag{3}$$

Table 1 Parameters at the flux surface $r \simeq 0.6a$ in the standard and inward-shifted configurations.

	q	r/R_0	ϵ_t	ϵ_h/ϵ_t	ϵ_-/ϵ_t	ϵ_+/ϵ_t
standard	1.9	0.099	0.087	0.91	-0.28	0
inward	1.7	0.114	0.082	1.20	-0.74	-0.24
	s	$r\epsilon'_{00}/\epsilon_t$	$r\epsilon'_t/\epsilon_t$	$r\epsilon'_h/\epsilon_t$	$r\epsilon'_-/\epsilon_t$	$r\epsilon'_+/\epsilon_t$
standard	-0.85	0.22	1.02	1.96	-0.63	0
inward	-0.96	0.71	1.00	2.44	-0.36	-0.61

where

$$\begin{aligned}\epsilon_T(r,\theta) &= \epsilon_{10}(r)\cos\theta+\epsilon_{L0}(r)\cos(L\theta),\\ \epsilon_H(r,\theta) &= \sqrt{C^2(r,\theta)+D^2(r,\theta)},\\ \chi_H(r,\theta) &= \arctan[D(r,\theta)/C(r,\theta)],\\ C(r,\theta) &= \sum_{|n|\le n_{max}}\epsilon_h^{(n)}(r)\cos(n\theta),\\ D(r,\theta) &= \sum_{|n|\le n_{max}}\epsilon_h^{(n)}(r)\sin(n\theta),\end{aligned} \tag{4}$$

and M (L) is the toroidal (main poloidal) period number of the helical field. In the present work, we use $L = 2$ and $M = 10$ to consider the LHD configurations. Here, we assume that $L/(qM) \ll 1$. Multiple-helicity effects can be included in the function $\epsilon_H(r,\theta)$. Hereafter, we put $\epsilon_{L0} = 0$, $n_{max} = 1$, and $\epsilon_{00} = 0$ (but $\epsilon'_{00} \equiv d\epsilon_{00}/dr \neq 0$) in Eq. (3) at the radial position r that we consider.

In order to model the standard and inward-shifted LHD configurations, we use numerical values shown in Table I for the safety factor q, the magnetic shear parameter $\hat{s}$, the inverse aspect ration r/R_0, the Fourier components of the field strength ($\epsilon_t \equiv \epsilon_{10}, \epsilon_h \equiv \epsilon_h^{(0)}, \epsilon_- \equiv \epsilon_h^{(-1)}, \epsilon_+ \equiv \epsilon_h^{(+1)}$), and their radial derivatives. The two sets of parameters in Table I for the standard and inward-shifted configurations are called S-B an I-B, respectively, in [15]. These parameters correspond to the flux surface at $r \simeq 0.6a$ (a : the plasma surface label) and they are taken from the vacuum magnetic field data, which describe the LHD configurations more accurately than the model field used in our previous study [10, 11]. The use of vacuum field data is justified because low beta plasmas are considered here.

3 Linear Analyses of ITG Modes and Zonal Flows

In this section, the linearized version of Eq. (1) and the quasineutrality condition given by Eq. (2) are numerically solved by using the GKV code in order to obtain the linear dispersion relation for the ITG instability and the zonal-flow response to the initial perturbation in the standard and inward-shifted configurations with the parameters shown in Table I.

3.1 Linear ITG instability

Figure 1 shows real frequencies and growth rates of the linear ITG instability as a function of the normalized poloidal wave number $k_\theta \rho_{ti}$ where $\rho_{ti} \equiv v_{ti}/\Omega_i$ is the ion thermal gyroradius. Here, $\eta_i \equiv L_n/L_{Ti} = 3$, $L_n/R_0 = 0.3$, $T_e/T_i = 1$, $\alpha \equiv \zeta - q\theta = 0$, and the parameters in Table I are used. The real frequencies and growth rates for the inward-shifted configuration take similar values to those for the standard configuration. Compared with the results in our previous work [10, 11], where simple model field parameters are used, the difference in the growth rates between the standard and inward-shifted configurations are reduced because of changes in values of q, $\hat{s}$ and magnetic curvature although the maximum growth rate for the latter case is still larger than for the former case.

3.2 Zonal-flow response

Collisionless time dependence of the zonal-flow potential, which has the wave number vector $\mathbf{k}_\perp = k_r \nabla r$ perpendicular to the flux surface, is analytically derived as [9]

$$\begin{aligned}
&\frac{e\phi_{\mathbf{k}_\perp}(t)}{T_i} \\
&= \mathcal{K}(t)\frac{e\phi_{\mathbf{k}_\perp}(0)}{T_i} + \frac{1}{n_0\langle k_\perp^2\rho_{ti}^2\rangle}\int_0^t dt'\,\mathcal{K}(t-t') \\
&\quad\times\left\{1 - \frac{2}{\pi}\left\langle (2\epsilon_H)^{1/2}\{1 - g_{i1}(t-t',\theta)\}\right\rangle\right\}^{-1} \\
&\quad\times\left\langle \int_{\kappa^2<1} d^3v\, e^{-ik_r\overline{v}_{dri}(t-t')}\, F_{i0} S_{i\mathbf{k}_\perp}(t') \right. \\
&\quad\left. + \int_{\kappa^2>1} d^3v\, F_{i0} S_{i\mathbf{k}_\perp}(t')\left\{1 + ik_r\left(\Delta_r - \langle\Delta_r\rangle_{\rm po}\right)\right\}\right\rangle,
\end{aligned} \tag{5}$$

where $\mathcal{K}(t)$ is defined by

$$\mathcal{K}(t) = \mathcal{K}_{GAM}(t)[1 - \mathcal{K}_L(0)] + \mathcal{K}_L(t). \tag{6}$$

Here, $\mathcal{K}_{GAM}(t)$ and $\mathcal{K}_L(t)$ are written as

$$\mathcal{K}_{GAM}(t) = \cos(\omega_G t)\exp(\gamma t), \tag{7}$$

and

$$\mathcal{K}_L(t) \equiv \frac{1 - (2/\pi)\langle (2\epsilon_H)^{1/2}\{1 - g_{i1}(t,\theta)\}\rangle}{1 + G + \mathcal{E}(t)/\left(n_0\langle k_\perp^2\rho_{ti}^2\rangle\right)}, \tag{8}$$

respectively. Detailed definitions of variables in Eqs. (5)–(8) are found in [9]. In Eq. (7), the real frequency and damping rate of the geodesic acoustic mode (GAM) [19] are denoted by ω_G and $|\gamma| = -\gamma(> 0)$. Equation (6) represents that the GAM oscillations described by $\mathcal{K}_{GAM}(t)$ are superimposed around the averaged zonal-flow evolution expressed by $\mathcal{K}_L(t)$. We note that $\mathcal{K}(0) = 1$ and $\lim_{t\to+\infty}\mathcal{K}_{GAM}(t) = 0$. In Eq. (8), G represents the ratio of the neoclassical polarization due to toroidally trapped ions to the classical polarization while $\mathcal{E}(t)$ and $\{1 - g_{i1}(t,\theta)\}$ are associated with the shielding caused by the radial drift of non-adiabatic helically trapped particles. We have $\mathcal{E} = 0$ and $g_{i1} = 1$ at $t = 0$ because helically trapped particles give no shielding before they begin radial drift. On the other hand, $\mathcal{E}$ approaches a finite value and $g_{i1} \simeq 0$ for $t \gg \tau_c = 1/(k_r v_{dr})$ where τ_c represents the characteristic time for the shielding due to helically-trapped particles to occur. The response kernel $\mathcal{K}_L(t)$ for the long-time behavior of the zonal-flow potential takes the constant limiting values,

$$\mathcal{K}_< \equiv \lim_{t/\tau_c\to+0}\mathcal{K}_L(t) = \frac{1}{1+G}, \tag{9}$$

and

$$\begin{aligned}
\mathcal{K}_> &\equiv \lim_{t/\tau_c\to+\infty}\mathcal{K}_L(t) \\
&= \langle k_\perp^2\rho_{ti}^2\rangle\left[1 - (2/\pi)\langle(2\epsilon_H)^{1/2}\rangle\right] \\
&\quad\times\left\{\langle k_\perp^2\rho_{ti}^2\rangle[1 - (3/\pi)\langle(2\epsilon_H)^{1/2}\rangle + G] \right. \\
&\quad\left. + (2/\pi)(1 + T_i/T_e)\langle(2\epsilon_H)^{1/2}\rangle\right\}^{-1}.
\end{aligned} \tag{10}$$

In Eq. (10), the term proportional to T_i/T_e is derived from taking account of the radial drift of helical-ripple-trapped electrons which cannot be described by the perturbed electron density model used in Eq. (2). Therefore, this term should be neglected when using Eq. (10) for comparison to numerical solutions of Eqs. (1) and (2).

Responses of the zonal-flow potential to the initial perturbation $\mathcal{K}(t) = \langle\phi_{\mathbf{k}_\perp}(t)\rangle/\langle\phi_{\mathbf{k}_\perp}(0)\rangle$ obtained by the linear gyrokinetic simulation for the standard and inward-shifted configurations are shown in Fig. 2, where the initial condition for the perturbed ion gyrocenter distribution function is given by $f_{i\mathbf{k}_\perp}(t=0) = n_{\mathbf{k}_\perp}(t=0)\exp(-m_i v^2/2T_i)$ with $n_{\mathbf{k}_\perp}(t=0)$ determined from $\phi_{\mathbf{k}_\perp}(t=0)$ through Eq. (2). Figure 2 also shows $\mathcal{K}_L(t)$ predicted by Eq. (8) for comparison to simulation results. We see that the change in the zonal-flow response $\mathcal{K}(t) = \langle\phi_{\mathbf{k}_\perp}(t)\rangle/\langle\phi_{\mathbf{k}_\perp}(0)\rangle$ between the standard and inward-shifted configurations are well described by $\mathcal{K}_L(t)$ except for the GAM oscillations. In order to measure the change in the zonal-flow response, we define the zonal-flow decay time as

$$\tau_{ZF} \equiv \int_0^{t_f}\langle\phi_{\mathbf{k}_\perp}(t)\rangle/\langle\phi_{\mathbf{k}_\perp}(0)\rangle, \tag{11}$$

where t_f represents the time at which the zonal flow reaches the final residual level and $t_f = 24R_0/v_{ti}$ is used in the present cases. Then, the simulation results give $\tau_{ZF} = 1.68\ R_0/v_{ti}$ for the inward-shifted case which is about 65% larger than $\tau_{ZF} = 1.02\ R_0/v_{ti}$ for the standard case. The increase in τ_{ZF} is attributed to the decrease in radial drift velocities of helical-ripple-trapped particles and the resultant delay in their shielding of the zonal-flow potential in the inward-shifted configuration. The improvement of the zonal-flow response due to the inward plasma shift was also found in our previous work [10, 11] using simpler configuration models although the degree of the improvement is more evident in the present study (see [15]).

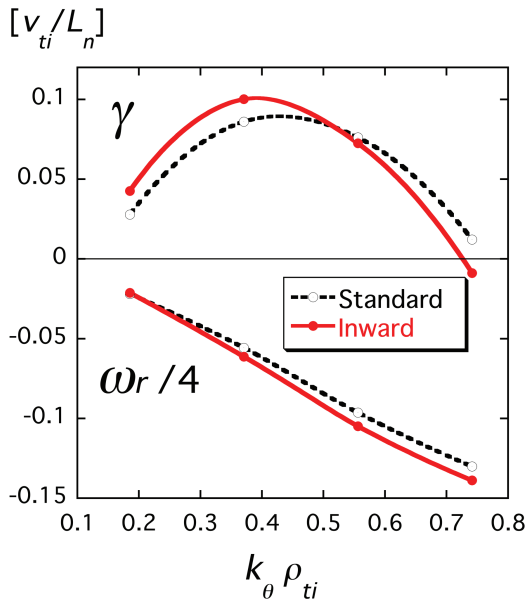

Fig. 1 Real frequencies and growth rates of the linear ITG instability as a function of the normalized poloidal wave number $k_\theta \rho_{ti}$ for the standard and inward-shifted configurations. Here, $\eta_i \equiv L_n/L_{Ti} = 3$, $L_n/R_0 = 0.3$, $T_e/T_i = 1$, $\alpha = 0$, and the parameters in Table I are used.

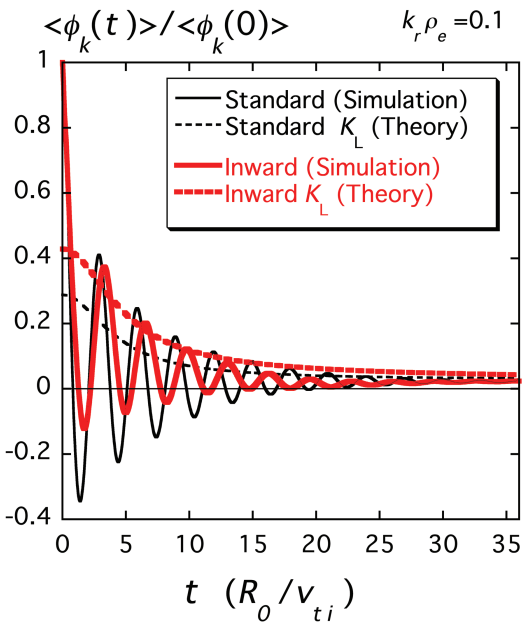

Fig. 2 Time evolution of the zonal-flow potential for the standard and inward-shifted configurations. Here, $k_r\rho_{ti} = 0.1$ is used. Solid curves are obtained from the linear gyrokinetic simulation. Dashed curves correspond to the long-time zonal-flow response kernel $K_L(t)$ in Eq. (8) which does not include the GAM oscillations.

4 Nonlinear Simulation of ITG Turbulence and Zonal Flows

This section presents nonlinear simulation results of the ITG turbulence and zonal flows obtained by solving Eqs. (1) and (2) with the GKV code (see also [16]). The GKV code employs the toroidal flux tube domain and we here use the same local plasma parameters ($\eta_i \equiv L_n/L_{Ti} = 3$, $L_n/R_0 = 0.3$, $T_e/T_i = 1$, and $\alpha = 0$) as in the linear calculations in Sec. 3.1. Figure 3 shows the turbulent ion thermal diffusivity χ_i as a function of time t obtained by the GKV simulation with the magnetic field data in Table I used for the standard and inward-shifted configurations. We see that, as expected from the results in Sec. 3.1, χ_i grows faster for the inward-shifted configuration in the early time stage ($t < 40L_n/v_{ti}$) than for the standard configuration and the peak value $\chi_i \simeq 3.8\rho_{ti}^2 v_{ti}/L_n$ for the former case is about 50% larger than the peak value $\chi_i \simeq 2.6\rho_{ti}^2 v_{ti}/L_n$ for the latter case. However, in later time ($t > 60L_n/v_{ti}$), the turbulent transport reaches statistically steady states and then the average ion thermal diffusivity $\chi_i \simeq 1.45\rho_{ti}^2 v_{ti}/L_n$ for the inward-shifted case is about 20% smaller than the average value $\chi_i \simeq 1.78\rho_{ti}^2 v_{ti}/L_n$ for the standard case. This reversal of the χ_i-value order results from a greater amount of zonal flows generated by turbulence in the inward-shifted plasma as seen below.

The GKV simulation shows that radially-elongated eddy structures (streamers) are first driven by the toroidal ITG instability although they are destroyed into small eddies by the self-generated $\mathbf{E} \times \mathbf{B}$ zonal flows in the later steady turbulent state [16]. The time-averaged spectrum of the zonal-flow potential ϕ_{k_x} is plotted in Fig. 4. It is found that the zonal-flow amplitude for $k_r\rho_{ti} \simeq 0.25$ in the inward-shifted configuration is about three times larger than that in the standard configuration. The stronger zonal-flow generation in the inward-shifted case is consistent with the larger zonal-flow decay time as mentioned in Sec. 3.2. A typical radial scale length of the zonal flows observed in the helical ITG simulations is shown to be shorter than those found in the tokamak ITG case for the Cyclone DIII-D base case parameters. Accordingly, the zonal-flow potential spectrum in the low k_r-region has relatively smaller amplitude than for the tokamak case. This tendency is also expected from the k_r-dependence of the zonal-flow response expressed in Eqs. (8) and (10).

5 Effects of Equilibrium Radial Electric Fields on Zonal Flows

So far, we have neglected effects of the equilibrium electrostatic potential $\Phi(r)$ which yields the radial electric field $\mathbf{E} = E_r \nabla r$ ($E_r = -d\Phi/dr$) and accordingly the $\mathbf{E} \times \mathbf{B}$ drift velocity $\mathbf{v}_E \equiv (c/B)E_r \nabla r \times \mathbf{b}$ in the direction tangential to the flux surface. Regarding the ITG modes, $\mathbf{v}_E$ will just give the Doppler shift $\mathbf{k}_\perp \cdot \mathbf{v}_E$ to the real frequencies without changing the growth rates. For the zonal-flow components with $\mathbf{k}_\perp = k_r \nabla r$, at first, the equilibrium electric field does not seem to influence the zonal-flow response

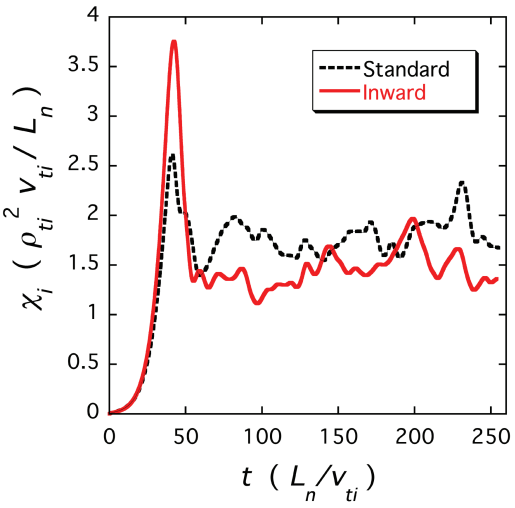

Fig. 3 Time evolution of the ion thermal diffusivity χ_i obtained by the ITG turbulence simulations for the standard and inward-shifted configurations.

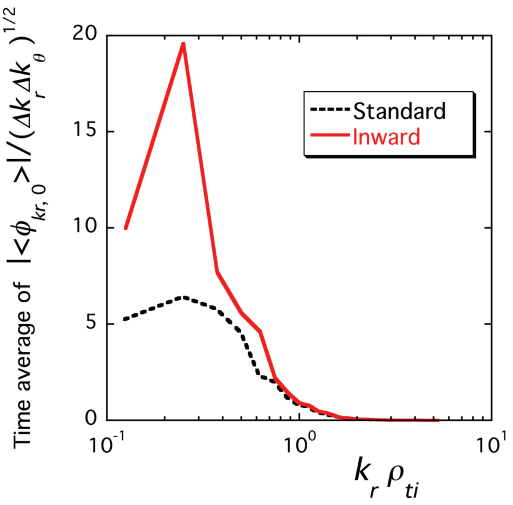

Fig. 4 Time-averaged radial-wave-number spectrum of the zonal-flow potential obtained by the ITG turbulence simulations for the standard and inward-shifted configurations. The time average is taken over $60 \le v_{ti}t/L_n \le 250$.

because $\mathbf{k}_\perp \cdot \mathbf{v}_E = 0$. However, when treating helical configurations, we find subtle points about the above argument with respect to the zonal-flow response. In the previous sections, we have used the ballooning representation and the local flux tube model, in which only the neighborhood of a single field line labeled by $\alpha \equiv \zeta - q(r)\theta$ is considered. For helical systems, the field line label α explicitly appears in the gyrokinetic equation in contrast to tokamak cases although we have so far regarded α as a fixed parameter based on the above-mentioned local model. But, even if the zonal-flow potential ϕ is independent of α, the explicit appearance of α in the magnetic drift terms of the gyrokinetic equation causes the perturbed gyrocenter distribution function δf to depend on α. Therefore, in helical configurations, we generally have $\mathbf{v}_E \cdot \nabla \delta f \neq 0$ so that the zonal-flow response can be affected by the existence of the equilibrium electric field.

Compared with passing and toroidally trapped particles, helical-ripple-trapped particles will have their orbits changed more greatly by the equilibrium radial electric field E_r. The radial displacements of helical-ripple-trapped particles are significantly reduced when the $\mathbf{E} \times \mathbf{B}$ drift due to E_r generates their rapid poloidal rotations as shown in Fig. 5. For such cases, neoclassical ripple transport is reduced and, in addition, higher zonal-flow responses are expected because the shielding of the zonal-flow potential by the helically-trapped particles is weakened. This scenario was first presented by Mynick and Boozer [17], who employed the action-angle formalism and pointed out the analogy between the mechanisms of zonal-flow shielding and neoclassical transport.

Taking account of the dependence of the perturbed distribution function on the field line label α, our formulation of zonal-flow response is extended to derive detailed expressions for the E_r effects on the zonal-flow response. We now assume the bounce centers of helically-trapped particles to draw poloidally-closed orbits with the poloidal angular velocity $\omega_\theta \equiv -cE_r/(rB_0)$. Furthermore, considering the helical configuration with the single-helicity component, for which $\epsilon_H = \epsilon_h$ is independent of θ, we find that, for $t \gg 1/\omega_\theta$, the shielding term $\mathcal{E}$ due to the helically-trapped particles in Eq. (8) is replaced with $\mathcal{E}_{Er}$ defined by

$$\mathcal{E}_{Er} = \frac{15}{8\pi}(2\epsilon_h)^{1/2}(k_r\rho_{ti})^2\left(\frac{\epsilon_t v_{ti}}{r\omega_\theta}\right)^2\left(1+\frac{T_e}{T_i}\right) \qquad (12)$$

Using Eq. (12), the collisionless long-time limit of the zonal-flow response kernel, which represents the residual zonal flow level, is now given not by Eq. (10) but by

$$\mathcal{K}_{Er} = \frac{1}{1+G+\mathcal{E}_{Er}/(k_r\rho_{ti})^2} = \left[1+G+\frac{15}{8\pi}(2\epsilon_h)^{1/2}\left(\frac{\epsilon_t v_{ti}}{r\omega_\theta}\right)^2\left(1+\frac{T_e}{T_i}\right)\right]^{-1} \qquad (13)$$

We see that, as E_r increases, $\mathcal{K}_{Er}$ increases and approaches the same value $1/(1+G)$ as in Eq. (9) because $\mathcal{E}_{Er}$ is inversely proportional to the square of E_r. It is noted that $\mathcal{E}_{Er}/k_r^2$ given from Eq. (12) corresponds to the product of the helically-trapped-particles' fraction ($\sim \epsilon_h^{1/2}$) and the square of the radial orbit width $\Delta_E (\propto 1/\omega_\theta \propto 1/E_r)$ of helically-trapped-particles' poloidal rotation (see Fig. 5), which agrees with Mynick and Boozer [17]. In helical configurations such as the inward-shifted LHD case, which are optimized for reduction of neoclassical transport, the enhancement of zonal-flow response due to E_r is expected to work more effectively than in others because the neoclassical optimization reduces radial displacements Δ_E of helically-trapped particles during their poloidal $\mathbf{E} \times \mathbf{B}$ rotation.

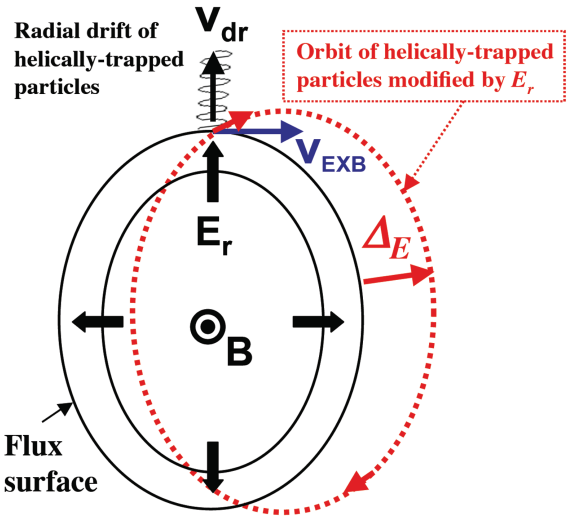

Fig. 5 Orbit of bounce-center motion of helical-ripple-trapped particles modified by the radial electric field E_r. Here, Δ_E represents the radial displacement of the orbit.

6 Conclusions

In the present work, effects of changes in helical magnetic configuration on anomalous transport and zonal flows are investigated based on gyrokinetic theory and simulation of ITG turbulence and zonal flows. In order to represent a specific flux surface ($r \simeq 0.6a$) in the standard and inward-shifted LHD configurations, magnetic parameters such as the Fourier components of the field strength, their radial derivatives, the safety factor, and the magnetic shear are used, which describe the configurations more accurately than our previous model parameters. We find from the linear analyses that the largest growth rate of the linear ITG instability for the inward-shifted configuration is slightly higher than that in the standard one while, for the former case, the zonal-flow response is more favorable to generation of low-frequency zonal flows because of lower radial drift velocities of helical-ripple-trapped particles than for the latter as theoretically predicted. The nonlinear gyrokinetic simulation shows that the turbulent ion thermal diffusivity χ_i for the inward-shifted plasma takes a higher peak value in the early time stage but a lower average value in the later steady turbulent state with stronger zonal-flow generation. Thus, it is confirmed that neoclassical optimization contributes to reduction of the anomalous transport by enhancing the zonal-flow level. This presents a physical mechanism to explain the confinement improvement observed in the LHD experiments with the inward plasma shift. Also, further enhancement of zonal flows and resultant transport reduction are theoretically expected when the equilibrium radial electric field E_r causes poloidal $\mathbf{E} \times \mathbf{B}$ rotation of helically-trapped particles with reduced radial displacements. Simulation studies on the E_r effects require global treatment in the direction parallel to the $\mathbf{E} \times \mathbf{B}$ drift velocity and remain as a future task.

Acknowledgments

This work is supported in part by the Japanese Ministry of Education, Culture, Sports, Science and Technology, Grant Nos. 16560727, 17360445, and 17·05373, and in part by the NIFS Collaborative Research Program, NIFS06KDAD006, NIFS06KNXN060 and NIFS06KTAT038. Numerical simulations were carried out with the use of the Earth Simulator under the support from the Japan Agency for Marine-Earth Science and Technology, and with the use of the Plasma Simulator and the LHD numerical analysis system at the National Institute for Fusion Science.

[1] P. H. Diamond, S.-I. Itoh, K. Itoh, and T. S. Hahm, Plasma Phys. Controlled Fusion **47**, R35 (2005).
[2] K. Itoh, S.-I. Itoh, P. H. Diamond, *et al.*, Phys. Plasmas **13**, 055502 (2006).
[3] M. Yokoyama, J. Plasma Fusion Res. **78**, 205 (2002).
[4] H. E. Mynick, Phys. Plasmas **13**, 058102 (2006).
[5] D. A. Spong, S. P. Hirshman, L. A. Berry, *et al.*, Nucl. Fusion **41**, 711 (2001).
[6] J. N. Talmadge, V. Sakaguchi, F. S. B. Anderson, *et al.*, Phys. Plasmas **9**, 5165 (2001).
[7] G. Grieger, W. Lotz, P. Merkel, *et al.*, Phys. Fluids B **4**, 2081 (1992).
[8] H. Sugama and T.-H. Watanabe, Phys. Rev. Lett. **94**, 115001 (2005).
[9] H. Sugama and T.-H. Watanabe, Phys. Plasmas **13**, 012501 (2006); H. Sugama and T.-H. Watanabe, *ibid.* **14**, 079902 (2007).
[10] T.-H. Watanabe and H. Sugama, 21th IAEA Fusion Energy Conference (Chengdu, China, 2006), EX/5-4.
[11] T.-H. Watanabe, H. Sugama, and S. Ferrando-Margalet, Nucl. Fusion **47**, 1383 (2007).
[12] O. Motojima, N. Ohyabu, A. Komori, *et.al.*, Nucl. Fusion **43**, 1674 (2003).
[13] H. Yamada, *et al.*, Plasma Phys. Controlled Fusion **43**, A55 (2001).
[14] T.-H. Watanabe and H. Sugama, Nucl. Fusion **46**, 24 (2006).
[15] S. Ferrando-Margalet, H. Sugama, and T.-H. Watanabe, "*Zonal flows and ion temperature gradient instabilities in multiple-helicity magnetic fields*", to be published in Phys. Plasmas.
[16] T.-H. Watanabe, H. Sugama, and S. Ferrando-Margalet, *Joint Conference of 17th International Toki Conference on Physics of Flows and Turbulence in Plasmas and 16th International Stellarator/Heliotron Workshop 2007* (Toki, Japan, 2007), P2-06.
[17] H. E. Mynick and A. H. Boozer, Phys. Plasmas **14**, 072507 (2007).
[18] K. C. Shaing and S. A. Hokin, Phys. Fluids **26**, 2136 (1983).
[19] N. Winsor, J. L. Johnson, and J. J. Dawson, Phys. Fluids **11**, 2248 (1968).